



SPECIAL ISSUE: Advanced Materials for Photoelectrochemical Cells

Novel Cu₃P/g-C₃N₄ p-n heterojunction photocatalysts for solar hydrogen generation

Zhixiao Qin, Menglong Wang, Rui Li and Yubin Chen*

ABSTRACT Developing efficient heterostructured photocatalysts to accelerate charge separation and transfer is crucial to improving photocatalytic hydrogen generation using solar energy. Herein, we report for the first time that p-type copper phosphide (Cu₃P) coupled with n-type graphitic carbon nitride (g-C₃N₄) forms a p-n junction to accelerate charge separation and transfer for enhanced photocatalytic activity. The optimized Cu₃P/g-C₃N₄ p-n heterojunction photocatalyst exhibits 95 times higher activity than bare g-C₃N₄, with an apparent quantum efficiency of 2.6% at 420 nm. A detail analysis of the reaction mechanism by photoluminescence, surface photovoltaics and electrochemical measurements revealed that the improved photocatalytic activity can be ascribed to efficient separation of photo-induced charge carriers. This work demonstrates that p-n junction structure is a useful strategy for developing efficient heterostructured photocatalysts.

Keywords: photocatalysis, copper phosphide, p-n junction, heterostructure, hydrogen production

INTRODUCTION

Hydrogen is considered to be an ideal energy source to substitute fossil fuel due to its high energy capacity and environmental friendliness [1]. Since the discovery of the Honda-Fujishima effect in 1972 [2], photocatalytic hydrogen production from water has attracted much attention as an ideal solution to global energy and environmental issues [3–6]. Developing highly active, long-term stable and low-cost photocatalysts is still a key to their commercial application. Recently, graphitic carbon nitride (g-C₃N₄) has emerged as an attractive metal-free polymeric semiconductor for photocatalytic hydrogen generation due to its specific laminar structure, high

stability and capability of visible-light harvest [7–11]. However, the severe photo-induced charge recombination and surface reaction still restrict the photocatalytic performance. Loading suitable cocatalysts seems to be a useful approach to boost photocatalytic hydrogen generation [12–14]. To date, Pt has been widely utilized as an efficient cocatalyst with g-C₃N₄, leading to significantly improved performances [15]. However, the high cost and low reserve of Pt limit the large-scale application and hence the development of non-precious photocatalytic system is quite appealing.

Recently, it has been demonstrated that a series of transition-metal phosphides could promote the photocatalytic hydrogen generation superior to g-C₃N₄ as cocatalysts [16–19]. For instance, our previous work demonstrated that Ni₂P cocatalyst could significantly increase photocatalytic performance for hydrogen generation over g-C₃N₄ [16]. Jiang *et al.* [17] reported that CoP was also an efficient cocatalyst to enhance the photocatalytic activity of g-C₃N₄. Besides g-C₃N₄, the photocatalytic properties of various semiconductor photocatalysts such as CdS [20–22], TiO₂ [16,23], and Cd_xZn_{1-x}S [24] could also be increased by coupling with transition-metal phosphides. However, the reported reaction mechanisms of these transition-metal phosphides are quite different. It is necessary to investigate more general coupling principle between photocatalysts and transition-metal phosphides as a guidance to develop efficient noble-metal-free hybrid photocatalysts.

Coupling semiconductors with different band structures to form heterojunction structure has been proved to be an effective way to promote the charge separation and photocatalytic performance [24–26]. When p-type semiconductor is combined with n-type semiconductor, a

International Research Center for Renewable Energy, State Key Laboratory of Multiphase Flow in Power Engineering, Xi'an Jiaotong University, Xi'an 710049, China

* Corresponding author (email: ybchen@mail.xjtu.edu.cn)

built-in electric field is achieved across the p-n junction region, which can efficiently promote the separation of photo-induced charges [27]. Copper phosphide (Cu_3P) is a p-type semiconductor with a band gap of 1.5 eV [23]. Due to its low cost and earth-abundant elements, Cu_3P was previously reported for application in lithium ion batteries [28–30]. However, the utilization of Cu_3P in photocatalytic hydrogen generation is still limited. Herein, we report a novel and low-cost $\text{Cu}_3\text{P}/\text{g-C}_3\text{N}_4$ p-n heterojunction photocatalyst for highly efficient hydrogen generation. Nanoscale p-n junctions developed in the hybrid photocatalysts could efficiently improve the photo-induced charge separation, leading to the significantly enhanced photocatalytic performance.

EXPERIMENTAL SECTION

Synthesis procedure

All chemicals in the present study are of analytical grade and used as received without further purification. $\text{g-C}_3\text{N}_4$ was synthesized by heating 10 g of urea at 550°C for 2 h in the air to obtain yellow powder. In a typical synthesis, $\text{Cu}(\text{OH})_2/\text{g-C}_3\text{N}_4$ was prepared by a simple precipitation method. 0.4 g of $\text{g-C}_3\text{N}_4$ was dispersed in 100 mL of 0.25 mol L⁻¹ NaOH aqueous solution, and then $\text{Cu}(\text{NO}_3)_2 \cdot 3\text{H}_2\text{O}$ was added under stirring. The mixed solution was stirred for 6 h at room temperature. The products were collected and washed three times with deionized water and ethanol. Then the precipitates were dried in a vacuum oven at 80°C for 5 h. Finally, $\text{Cu}_3\text{P}/\text{g-C}_3\text{N}_4$ photocatalyst was synthesized through a solid-state reaction. Typically, 0.2 g of the prepared $\text{Cu}(\text{OH})_2/\text{g-C}_3\text{N}_4$ and 0.1 g of NaH_2PO_2 were blended mechanically and ground into fine power. Then, the fine power was annealed at 300°C for 2 h in a quartz tube with a heating rate of 5 °C min⁻¹ under Ar flow. The obtained products were washed with deionized water to remove residual salts, and dried under vacuum at 50°C. The Cu_3P was also prepared using a similar procedure. The loading weight of Cu_3P in $\text{Cu}_3\text{P}/\text{g-C}_3\text{N}_4$ was measured by X-ray photoelectron spectroscopy (XPS) analysis and the results were shown in Table S1. The practical loading concentrations of Cu_3P were close to the theoretical values.

Characterization

X-ray powder diffraction (XRD) patterns were obtained from a PANalytical X'pert MPD Pro X-ray diffractometer. Transmission electron microscopy (TEM) images were obtained using a FEI Tecnai G2 F30 S-Twin microscope attached with an OXFORD MAX-80 energy

dispersive X-ray (EDX) system. UV-visible (UV-vis) absorption spectra were measured on a HITACHI U4100 spectrophotometer. XPS measurements were conducted on a Kratos Axis-Ultra multifunctional X-ray spectrometer. All binding energies were referenced to the C 1s peak at 284.8 eV. Photoluminescence (PL) spectra were examined using a PTI QM-4 fluorescence spectrophotometer with an excitation wavelength of 320 nm. The lock-in-based surface photovoltage (SPV) spectra were obtained using a surface photovoltage spectroscope. The measurement system consists of a source of monochromatic light (Omni- λ 300), a lock-in amplifier (SR830) with a light chopper (SR540), and a sample chamber.

Visible-light-driven photocatalytic measurement

Photocatalytic hydrogen generation was performed in a side irradiation Pyrex cell with a magnetic stirring. Typically, 20 mg of the as-prepared photocatalyst was added into 80 mL of aqueous solution containing 10 vol% triethanolamine (TEOA) as the electron donors. Before irradiation, nitrogen was purged into the reaction cell for 30 min to remove air in the dark. The reaction temperature was kept at 35°C. A 300 W Xe-lamp equipped with a 420 nm cutoff filter was employed to provide the visible-light irradiation. The amount of generated hydrogen was measured by gas chromatography using a thermal conductivity detector (TCD). The apparent quantum efficiency (AQE) could be calculated as $\text{AQE}(\%) = (\text{the number of evolved hydrogen molecules} \times 2 / \text{the number of incident photons}) \times 100\%$.

RESULTS AND DISCUSSION

Physicochemical properties of $\text{Cu}_3\text{P}/\text{g-C}_3\text{N}_4$ heterostructure

The crystal structures of the as-prepared samples were investigated by XRD. As shown in Fig. 1, two distinct diffraction peaks of bare $\text{g-C}_3\text{N}_4$ could be attributed to the graphitic phase with tri-s-triazine units. The Cu_3P sample shows diffraction peaks located at 36.0°, 39.0°, 41.5°, 45.1°, and 46.2°, corresponding to the (112), (202), (211), (300), and (213) planes of hexagonal Cu_3P (PDF#71-2261) [22]. It has been reported that trace amount of Cu was involved in the Cu_3P sample, which was prepared *via* a phosphatization method [23]. The main diffraction peaks of $\text{Cu}_3\text{P}/\text{g-C}_3\text{N}_4$ could be attributed to the graphitic phase $\text{g-C}_3\text{N}_4$. There were not apparent peaks corresponding to Cu_3P , possibly due to the low amount and high dispersity.

We further investigated the morphology of $\text{g-C}_3\text{N}_4$ photocatalysts after loading Cu_3P . As displayed in Fig. 2a,

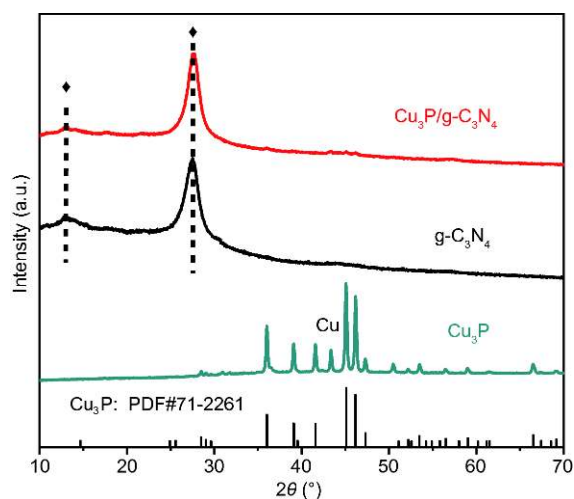


Figure 1 XRD patterns of Cu_3P , $\text{g-C}_3\text{N}_4$, and $\text{Cu}_3\text{P/g-C}_3\text{N}_4$.

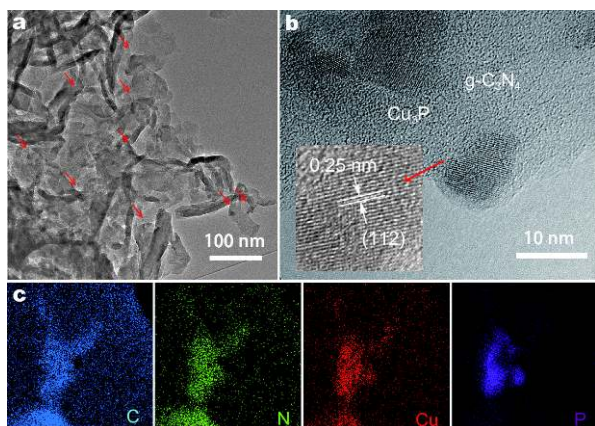


Figure 2 (a) TEM and (b) HRTEM images of $\text{Cu}_3\text{P/g-C}_3\text{N}_4$. (c) Elemental mapping of C, N, Cu, and P species in $\text{Cu}_3\text{P/g-C}_3\text{N}_4$ (excess C and Cu signals came from the carbon film on the copper grid).

the hybrid samples had uniformly dispersed Cu_3P nanoparticles anchored on the surface of $\text{g-C}_3\text{N}_4$ nanosheets (Fig. 2b). The lattice distance of 0.25 nm corresponded to the (112) plane of hexagonal Cu_3P . To determine the composition and element distribution of $\text{Cu}_3\text{P/g-C}_3\text{N}_4$, the elemental mapping of C, N, Cu, and P species was carried out (Fig. 2c). It was proved that Cu_3P nanoparticles were successfully distributed on the surface of $\text{g-C}_3\text{N}_4$. The specific surface area of $\text{Cu}_3\text{P/g-C}_3\text{N}_4$ was $70.2 \text{ m}^2 \text{ g}^{-1}$, which was close to that of single $\text{g-C}_3\text{N}_4$ ($73.1 \text{ m}^2 \text{ g}^{-1}$). This result indicated that the fabrication of hybrid samples did not lead to agglomeration of $\text{g-C}_3\text{N}_4$.

XPS measurements were performed to investigate the surface chemical states of $\text{Cu}_3\text{P/g-C}_3\text{N}_4$. As shown in Fig.

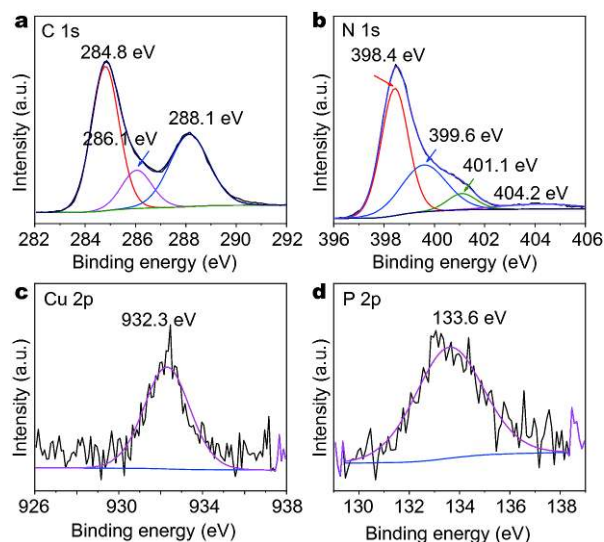


Figure 3 XPS spectra of $\text{Cu}_3\text{P/g-C}_3\text{N}_4$. (a) C 1s, (b) N 1s, (c) Cu 2p, and (d) P 2p.

3a, the typical values for C–C, C– NH_2 , and N–C=N in $\text{g-C}_3\text{N}_4$ were respectively presented at binding energies of 284.8, 286.1, and 288.1 eV [31]. Meanwhile, the peaks at 398.4, 399.6, 401.1, and 404.2 eV of N 1s spectrum (Fig. 3b) could be assigned to the binding energies of C–N=C, N–(C)₃, C–N–H, and π excitations of $\text{g-C}_3\text{N}_4$, respectively [24]. Fig. 3c shows the Cu 2p profile with a peak located at 932.3 eV, and the P 2p region has a single peak at 133.6 eV (Fig. 3d). The peak at 932.3 eV could be ascribed to Cu–P in Cu_3P , and the peak at 133.6 eV arose from oxidized P species probably due to the air exposure [23]. The XPS results further demonstrated the successful synthesis of Cu_3P and $\text{g-C}_3\text{N}_4$ in the heterostructure.

The optical properties of the as-prepared samples were measured by UV-vis spectrophotometer. As shown in Fig. 4a, the spectrum of bare $\text{g-C}_3\text{N}_4$ displayed a sharp edge at around 450 nm. After the coupling of Cu_3P onto the $\text{g-C}_3\text{N}_4$ surface, an increased absorption in visible range of 400–800 nm was observed. Meanwhile, the UV-vis absorption spectrum of pure Cu_3P (Fig. 4b) showed an apparent absorption from 300 to 800 nm. The absorption peak around 550 nm could be attributed to the plasmon peak of Cu nanoparticles in as-prepared Cu_3P sample [32]. The optical band gaps (E_g) of $\text{g-C}_3\text{N}_4$ and Cu_3P were estimated from Tauc plots of $(\alpha h\nu)^n$ vs. photon energy ($h\nu$) [33]. The insets show that the band gaps of $\text{g-C}_3\text{N}_4$ and Cu_3P were respectively determined to be 2.72 and 1.50 eV, which were consistent with the previous studies [23,34].

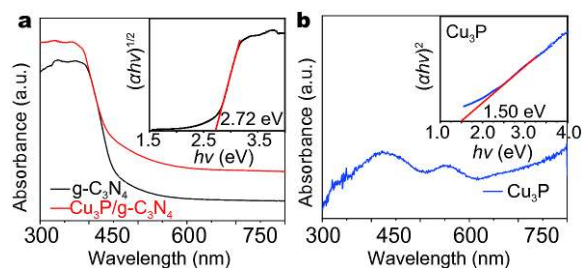


Figure 4 UV-vis absorption spectra of (a) $g\text{-C}_3\text{N}_4$, $\text{Cu}_3\text{P}/g\text{-C}_3\text{N}_4$ and (b) Cu_3P . The insets show the plots of $(\alpha hv)^{1/2}$ vs. photon energy ($h\nu$) for $g\text{-C}_3\text{N}_4$ and $(\alpha hv)^2$ vs. $h\nu$ for Cu_3P .

Photocatalytic hydrogen production

The photocatalytic hydrogen generation was subsequently investigated in triethanolamine (TEOA) aqueous solution under visible-light irradiation. As shown in Fig. 5a, the hydrogen production rate of bare $g\text{-C}_3\text{N}_4$ was rather low, and Cu_3P could significantly boost the photocatalytic hydrogen generation of $g\text{-C}_3\text{N}_4$. The rate of hydrogen generation initially increased and then decreased with increasing amount of Cu_3P . With the optimal loading amount of Cu_3P , $\text{Cu}_3\text{P}/g\text{-C}_3\text{N}_4$ showed the highest hydrogen production rate of $284 \mu\text{mol h}^{-1} \text{g}^{-1}$, which was about 95 times higher than that of bare $g\text{-C}_3\text{N}_4$. The apparent quantum efficiency (AQE) for hydrogen generation was calculated to be 2.6% at 420 nm. However, no appreciable hydrogen generation could be detected in bare Cu_3P , indicating that Cu_3P was not an active photocatalyst [22]. By comparison, the activity of physically mixed $\text{Cu}_3\text{P}@g\text{-C}_3\text{N}_4$ was measured under the same condition. The hydrogen production rate of $\text{Cu}_3\text{P}@g\text{-C}_3\text{N}_4$ was much lower than that of $\text{Cu}_3\text{P}/g\text{-C}_3\text{N}_4$, revealing that the intimate contact between Cu_3P and $g\text{-C}_3\text{N}_4$ takes effect on the performance [24]. Long-term photocatalytic test of $\text{Cu}_3\text{P}/g\text{-C}_3\text{N}_4$ for hydrogen generation was carried out to evaluate the stability of $\text{Cu}_3\text{P}/g\text{-C}_3\text{N}_4$ hybrid photocatalysts. As displayed in Fig. 5b, there was no apparent decrease in the photocatalytic activity over the 20 h reaction, indicating its good stability.

Mechanism study

PL spectra of the as-prepared samples were measured to explore the charge separation and migration behaviors in the photocatalyst. As shown in Fig. 6a, both $g\text{-C}_3\text{N}_4$ and $\text{Cu}_3\text{P}/g\text{-C}_3\text{N}_4$ exhibited broad emission peaks centered around 450 nm, corresponding to the band gap of $g\text{-C}_3\text{N}_4$. Compared to pure $g\text{-C}_3\text{N}_4$, $\text{Cu}_3\text{P}/g\text{-C}_3\text{N}_4$ showed apparently decreased PL intensity, which indicated that loading Cu_3P could facilitate the charge transfer so as to inhibit

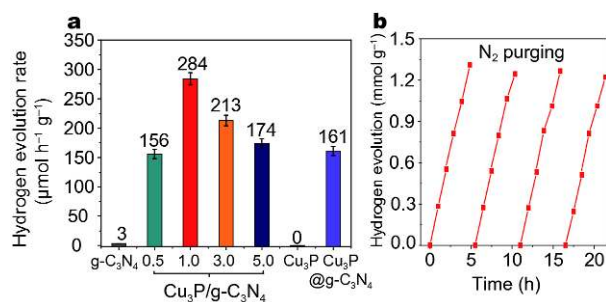


Figure 5 (a) Photocatalytic hydrogen evolution rates of $g\text{-C}_3\text{N}_4$, $\text{Cu}_3\text{P}/g\text{-C}_3\text{N}_4$ (the loading amount of Cu_3P was respectively 0.5, 1, 3, and 5 wt%), Cu_3P , and physically mixed $\text{Cu}_3\text{P}@g\text{-C}_3\text{N}_4$ (the loading amount of Cu_3P was 1 wt%). (b) Long-time photocatalytic test of 1 wt% $\text{Cu}_3\text{P}/g\text{-C}_3\text{N}_4$ sample for hydrogen evolution. (Reaction condition: 20 mg of photocatalysts, 80 mL of aqueous solution containing 10 vol% TEOA, 300 W Xe lamp equipped with a cutoff filter ($\lambda \geq 420 \text{ nm}$)).

the charge recombination in $g\text{-C}_3\text{N}_4$ [35], which was beneficial to photocatalytic performance.

The lock-in-based SPV spectra were also carried out to reveal the transfer properties of the photo-induced charge carriers. The signal of SPV can be attributed to the variation of surface potential barriers during the light irradiation, which can identify the light-responsive wavelength range and the separation efficiency of the electron-hole pairs in the photocatalysts [36]. As shown in Fig. 6b, positive photovoltaic responses ranging from 300 to 400 nm were observed for $g\text{-C}_3\text{N}_4$, indicating that $g\text{-C}_3\text{N}_4$ is a typical n-type semiconductor [37]. After loading Cu_3P on the surface of $g\text{-C}_3\text{N}_4$, the response signal of $\text{Cu}_3\text{P}/g\text{-C}_3\text{N}_4$ was obviously enhanced. The enhanced SPV signal intensity indicated that the introduction of Cu_3P was beneficial to the photo-induced charge separation in $\text{Cu}_3\text{P}/g\text{-C}_3\text{N}_4$ heterostructures [38].

In addition to the charge-transfer behavior in the photocatalyst, the charge-transfer at the photocatalyst/solution interface is also crucial to the photocatalytic performance. Therefore, $g\text{-C}_3\text{N}_4$ and $\text{Cu}_3\text{P}/g\text{-C}_3\text{N}_4$ electrodes were fabricated (see Supplementary information) and the electrochemical impedance spectroscopy (EIS) was performed to elucidate the charge-transfer resistances. As shown in Fig. 7a, the Nyquist impedance plots for the electrodes could be fitted to an equivalent circuit (the inset) consisting of the series resistance (R_s), charge transfer resistance from the electrode to the electrolyte (R_{ct}), recombination resistance at the electrode interface (R_{rec}), and constant phase elements (CPE1 and CPE2). As summarized in Table S2, the values of R_{ct} and R_{rec} for $\text{Cu}_3\text{P}/g\text{-C}_3\text{N}_4$ were lower than those of $g\text{-C}_3\text{N}_4$, indicating that the $\text{Cu}_3\text{P}/g\text{-C}_3\text{N}_4$ had efficient charge-

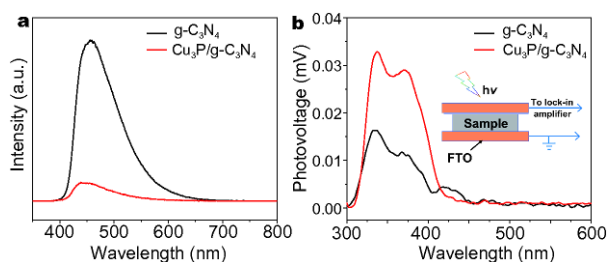


Figure 6 (a) PL spectra of g-C₃N₄ and Cu₃P/g-C₃N₄. (b) SPV spectra of g-C₃N₄ and Cu₃P/g-C₃N₄. The inset shows the schematic setup for the SPV measurement.

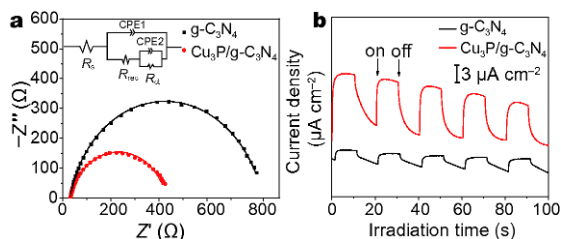


Figure 7 (a) Nyquist impedance plots of g-C₃N₄ and Cu₃P/g-C₃N₄ measured at -1.0 V vs. RHE in N₂-saturated 0.5 mol L^{-1} Na₂SO₄ aqueous solution. The inset shows the equivalent circuit. (b) Transient photocurrent responses of g-C₃N₄ and Cu₃P/g-C₃N₄ measured at 0.2 V vs. RHE in N₂-saturated 0.5 mol L^{-1} Na₂SO₄ aqueous solution. A 500 W Xe lamp coupled with an AM 1.5 filter was used as the light source for the photocurrent measurement.

transfer behavior at the photocatalyst/solution interface [16,39]. The transient photocurrent responses of g-C₃N₄ and Cu₃P/g-C₃N₄ were also investigated to examine their photoelectrochemical properties. As shown in Fig. 7b, Cu₃P/g-C₃N₄ exhibited a much higher photocurrent density than that of pure g-C₃N₄, suggesting a noticeable improvement in the suppression of charge recombination [40], which was consistent with PL and SPV results.

The spectroscopic and electrochemical analyses revealed that Cu₃P/g-C₃N₄ owns efficient charge separation, which is essential to achieve high photocatalytic activity. To better understand the photo-induced charge carrier dynamics involved in the Cu₃P/g-C₃N₄ heterojunction, the band alignment of Cu₃P and g-C₃N₄ were investigated. The valence band positions (E_{VB}) of Cu₃P and g-C₃N₄ were firstly measured by XPS valence band spectra. As displayed in Fig. 8a, b, the E_{VB} of Cu₃P and g-C₃N₄ were determined to be 0.71 and 1.74 eV, respectively. Since the band gaps (E_{g}) of Cu₃P and g-C₃N₄ were 1.50 and 2.72 eV, respectively, the conduction band positions (E_{CB}) of Cu₃P and g-C₃N₄ were calculated to be -0.79 and -0.98 eV, according to the equation: $E_{\text{VB}} = E_{\text{CB}} + E_{\text{g}}$ [41]. Mott-Schottky plot of g-C₃N₄ showed (Fig. 8c) a

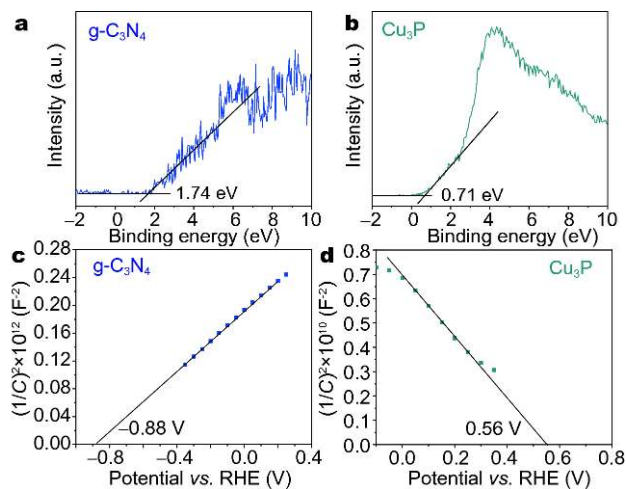


Figure 8 XPS valence band spectra for (a) g-C₃N₄ and (b) Cu₃P. Mott-Schottky plots of (c) g-C₃N₄ and (d) Cu₃P in N₂-saturated 0.5 mol L^{-1} Na₂SO₄ aqueous solution.

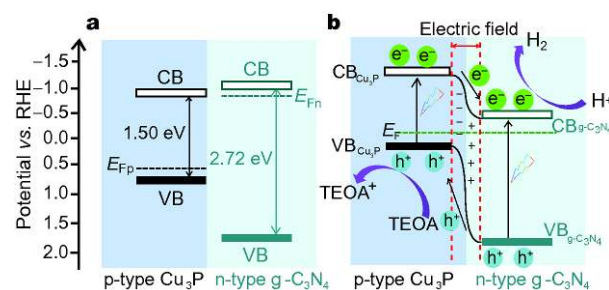


Figure 9 (a) Energy band structures of Cu₃P and g-C₃N₄ before formation of the heterojunction. (b) The band structure for Cu₃P/g-C₃N₄ heterojunction and charge separation process under illumination.

positive slope, indicating that it is an n-type semiconductor, while a negative slope of Cu₃P (Fig. 8d) corresponds to a p-type semiconductor [42]. The flat-band potentials of Cu₃P and g-C₃N₄ were estimated to be 0.56 and -0.88 V vs. RHE, which were close to the determined E_{VB} of Cu₃P and E_{CB} of g-C₃N₄. As shown in Fig. S1, Cu₃P/g-C₃N₄ exhibited the similar feature as pristine g-C₃N₄ owing to the low amount of Cu₃P. A positive slope was observed for Cu₃P/g-C₃N₄, and the flat band potential was determined to be -0.75 V vs. RHE, which was close to that of g-C₃N₄.

Therefore, the energy band structures of Cu₃P and g-C₃N₄ before forming the heterojunction are shown in Fig. 9a. The Fermi level (E_{F}) of g-C₃N₄ is higher than that of Cu₃P. When p-type Cu₃P is coupled with n-type g-C₃N₄, electrons will transfer from g-C₃N₄ to Cu₃P until the Fermi levels to be equal for both phases [43]. As shown in Fig. 9b, a built-in electric field is formed across the p-n

junction, where the p-type Cu_3P region is negatively charged, and the n-type $\text{g-C}_3\text{N}_4$ region is positively charged. When $\text{Cu}_3\text{P/g-C}_3\text{N}_4$ photocatalysts are irradiated with visible light, the photo-induced electrons and holes will be obtained in Cu_3P and $\text{g-C}_3\text{N}_4$. As a result of the built-in electric field, the photo-induced electrons in the CB of Cu_3P will diffuse into the CB of $\text{g-C}_3\text{N}_4$ through the p-n junction, giving rise to the accumulation of photo-induced electrons in $\text{g-C}_3\text{N}_4$. Meanwhile, the photo-induced holes in the VB of $\text{g-C}_3\text{N}_4$ will diffuse into the VB of Cu_3P , leading to the accumulation of photo-induced holes in Cu_3P . Subsequently, the accumulated photo-induced electrons can transfer to the surface of $\text{g-C}_3\text{N}_4$ to reduce H^+ for hydrogen production, and the accumulated photo-induced holes can migrate to the surface of Cu_3P to oxidize TEOA. As a consequence, the efficient charge separation is successfully achieved by the p-n junctions in hybrid $\text{Cu}_3\text{P/g-C}_3\text{N}_4$. During the photocatalytic reaction, Cu_3P captured the photo-induced holes in $\text{g-C}_3\text{N}_4$ and functioned as the active sites for the surface oxidation reaction.

CONCLUSIONS

In summary, $\text{Cu}_3\text{P/g-C}_3\text{N}_4$ heterostructures were successfully constructed to achieve the efficient separation of photo-induced charges. Cu_3P nanoparticles were tightly attached to the surface of $\text{g-C}_3\text{N}_4$, leading to the formation of p-n junctions between p-type Cu_3P and n-type $\text{g-C}_3\text{N}_4$. The p-n junctions could promote charge transfer and reduce charge recombination, leading to an enhanced photocatalytic activity. The optimized $\text{Cu}_3\text{P/g-C}_3\text{N}_4$ p-n heterojunction photocatalyst exhibits 95 times higher activity than bare $\text{g-C}_3\text{N}_4$, with an apparent quantum efficiency of 2.6% at 420 nm. This work proposes an effective guidance to develop efficient noble-metal-free hybrid photocatalysts by p-n junction structure.

Received 30 October 2017; accepted 28 November 2017;
published online 15 January 2018

- 1 Gray HB. Powering the planet with solar fuel. *Nat Chem*, 2009, 1: 7
- 2 Fujishima A, Honda K. Electrochemical photolysis of water at a semiconductor electrode. *Nature*, 1972, 238: 37–38
- 3 Chen X, Shen S, Guo L, et al. Semiconductor-based photocatalytic hydrogen generation. *Chem Rev*, 2010, 110: 6503–6570
- 4 Tong H, Ouyang S, Bi Y, et al. Nano-photocatalytic materials: possibilities and challenges. *Adv Mater*, 2012, 24: 229–251
- 5 Zhang K, Guo L. Metal sulphide semiconductors for photocatalytic hydrogen production. *Catal Sci Technol*, 2013, 3: 1672–1690
- 6 Su J, Zhou J, Wang L, et al. Synthesis and application of transition metal phosphides as electrocatalyst for water splitting. *Sci Bull*, 2017, 62: 633–644
- 7 Wang X, Maeda K, Thomas A, et al. A metal-free polymeric photocatalyst for hydrogen production from water under visible light. *Nat Mater*, 2009, 8: 76–80
- 8 Liu G, Wang T, Zhang H, et al. Nature-inspired environmental “phosphorylation” boosts photocatalytic H_2 production over carbon nitride nanosheets under visible-light irradiation. *Angew Chem*, 2015, 127: 13765–13769
- 9 Liu J, Liu Y, Liu N, et al. Metal-free efficient photocatalyst for stable visible water splitting via a two-electron pathway. *Science*, 2015, 347: 970–974
- 10 Li Y, Xu H, Ouyang S, et al. *In situ* surface alkalized $\text{g-C}_3\text{N}_4$ toward enhancement of photocatalytic H_2 evolution under visible-light irradiation. *J Mater Chem A*, 2016, 4: 2943–2950
- 11 Ong WJ, Tan LL, Ng YH, et al. Graphitic carbon nitride ($\text{g-C}_3\text{N}_4$)-based photocatalysts for artificial photosynthesis and environmental remediation: are we a step closer to achieving sustainability? *Chem Rev*, 2016, 116: 7159–7329
- 12 Qin Z, Chen Y, Wang X, et al. Intergrowth of cocatalysts with host photocatalysts for improved solar-to-hydrogen conversion. *ACS Appl Mater Interfaces*, 2016, 8: 1264–1272
- 13 Chang K, Mei Z, Wang T, et al. $\text{MoS}_2/\text{Graphene}$ cocatalyst for efficient photocatalytic H_2 evolution under visible light irradiation. *ACS Nano*, 2014, 8: 7078–7087
- 14 Yang J, Wang D, Han H, et al. Roles of cocatalysts in photocatalysis and photoelectrocatalysis. *Acc Chem Res*, 2013, 46: 1900–1909
- 15 Maeda K, Wang X, Nishihara Y, et al. Photocatalytic activities of graphitic carbon nitride powder for water reduction and oxidation under visible light. *J Phys Chem C*, 2009, 113: 4940–4947
- 16 Chen Y, Qin Z. General applicability of nanocrystalline Ni_2P as a noble-metal-free cocatalyst to boost photocatalytic hydrogen generation. *Catal Sci Technol*, 2016, 6: 8212–8221
- 17 Yi SS, Yan JM, Wulan BR, et al. Noble-metal-free cobalt phosphide modified carbon nitride: an efficient photocatalyst for hydrogen generation. *Appl Catal B-Environ*, 2017, 200: 477–483
- 18 Indra A, Acharjya A, Menezes PW, et al. Boosting visible-light-driven photocatalytic hydrogen evolution with an integrated nickel phosphide-carbon nitride system. *Angew Chem Int Ed*, 2017, 56: 1653–1657
- 19 Zhao H, Sun S, Jiang P, et al. Graphitic C_3N_4 modified by Ni_2P cocatalyst: an efficient, robust and low cost photocatalyst for visible-light-driven H_2 evolution from water. *Chem Eng J*, 2017, 315: 296–303
- 20 Sun Z, Zheng H, Li J, et al. Extraordinarily efficient photocatalytic hydrogen evolution in water using semiconductor nanorods integrated with crystalline Ni_2P cocatalysts. *Energy Environ Sci*, 2015, 8: 2668–2676
- 21 Cao S, Chen Y, Wang CJ, et al. Spectacular photocatalytic hydrogen evolution using metal-phosphide/CdS hybrid catalysts under sunlight irradiation. *Chem Commun*, 2015, 51: 8708–8711
- 22 Sun Z, Yue Q, Li J, et al. Copper phosphide modified cadmium sulfide nanorods as a novel p-n heterojunction for highly efficient visible-light-driven hydrogen production in water. *J Mater Chem A*, 2015, 3: 10243–10247
- 23 Yue X, Yi S, Wang R, et al. A novel and highly efficient earth-abundant Cu_3P with TiO_2 “P-N” heterojunction nanophotocatalyst for hydrogen evolution from water. *Nanoscale*, 2016, 8: 17516–17523
- 24 Qin Z, Xue F, Chen Y, et al. Spatial charge separation of one-dimensional $\text{Ni}_2\text{P-Cd}_{0.9}\text{Zn}_{0.1}\text{S/g-C}_3\text{N}_4$ heterostructure for high-quantum-yield photocatalytic hydrogen production. *Appl Catal B-*

- Environ*, 2017, 217: 551–559
- 25 Chen Y, Qin Z, Wang X, *et al.* Noble-metal-free Cu₂S-modified photocatalysts for enhanced photocatalytic hydrogen production by forming nanoscale p-n junction structure. *RSC Adv*, 2015, 5: 18159–18166
- 26 Chen Y, Wang L, Lu GM, *et al.* Nanoparticles enwrapped with nanotubes: a unique architecture of CdS/titanate nanotubes for efficient photocatalytic hydrogen production from water. *J Mater Chem*, 2011, 21: 5134–5141
- 27 Meng F, Li J, Cushing SK, *et al.* Solar hydrogen generation by nanoscale p-n junction of p-type molybdenum disulfide/n-type nitrogen-doped reduced graphene oxide. *J Am Chem Soc*, 2013, 135: 10286–10289
- 28 Manna G, Bose R, Pradhan N. Semiconducting and plasmonic copper phosphide platelets. *Angew Chem Int Ed*, 2013, 52: 6762–6766
- 29 Ni S, Ma J, Lv X, *et al.* The fine electrochemical performance of porous Cu₃P/Cu and the high energy density of Cu₃P as anode for Li-ion batteries. *J Mater Chem A*, 2014, 2: 20506–20509
- 30 Villeveille C, Robert F, Taberna PL, *et al.* The good reactivity of lithium with nanostructured copper phosphide. *J Mater Chem*, 2008, 18: 5956–5960
- 31 Liang Q, Li Z, Yu X, *et al.* Macroscopic 3D porous graphitic carbon nitride monolith for enhanced photocatalytic hydrogen evolution. *Adv Mater*, 2015, 27: 4634–4639
- 32 Xiong J, Wang Y, Xue Q, *et al.* Synthesis of highly stable dispersions of nanosized copper particles using L-ascorbic acid. *Green Chem*, 2011, 13: 900–904
- 33 Butler MA. Photoelectrolysis and physical properties of the semiconducting electrode WO₂. *J Appl Phys*, 1977, 48: 1914–1920
- 34 Zhang G, Lan ZA, Lin L, *et al.* Overall water splitting by Pt/g-C₃N₄ photocatalysts without using sacrificial agents. *Chem Sci*, 2016, 7: 3062–3066
- 35 Chen Z, Berciaud S, Nuckolls C, *et al.* Energy transfer from individual semiconductor nanocrystals to graphene. *ACS Nano*, 2010, 4: 2964–2968
- 36 Han C, Wu L, Ge L, *et al.* AuPd bimetallic nanoparticles decorated graphitic carbon nitride for highly efficient reduction of water to H₂ under visible light irradiation. *Carbon*, 2015, 92: 31–40
- 37 Bi L, Xu D, Zhang L, *et al.* Metal Ni-loaded g-C₃N₄ for enhanced photocatalytic H₂ evolution activity: the change in surface band bending. *Phys Chem Chem Phys*, 2015, 17: 29899–29905
- 38 Cao S, Low J, Yu J, *et al.* Polymeric photocatalysts based on graphitic carbon nitride. *Adv Mater*, 2015, 27: 2150–2176
- 39 Qin Z, Chen Y, Huang Z, *et al.* Composition-dependent catalytic activities of noble-metal-free NiS/Ni₃S₄ for hydrogen evolution reaction. *J Phys Chem C*, 2016, 120: 14581–14589
- 40 Zhang J, Qi L, Ran J, *et al.* Ternary NiS/Zn_xCd_{1-x}S/reduced graphene oxide nanocomposites for enhanced solar photocatalytic H₂-production activity. *Adv Energy Mater*, 2014, 4: 1301925
- 41 Chen J, Shen S, Guo P, *et al.* *In-situ* reduction synthesis of nanosized Cu₂O particles modifying g-C₃N₄ for enhanced photocatalytic hydrogen production. *Appl Catal B-Environ*, 2014, 152–153: 335–341
- 42 Chen Y, Qin Z, Chen T, *et al.* Optimization of (Cu₂Sn)_xZn_{3(1-x)}S₃/CdS pn junction photoelectrodes for solar water reduction. *RSC Adv*, 2016, 6: 58409–58416
- 43 Kronik L, Shapira Y. Surface photovoltage phenomena: theory, experiment, and applications. *Surf Sci Rep*, 1999, 37: 1–206

Acknowledgements The authors thank the financial support from the National Natural Science Foundation of China (21606175), the grant support from China Postdoctoral Science Foundation (2014M560768), and China Fundamental Research Funds for the Central Universities (xjj2015041).

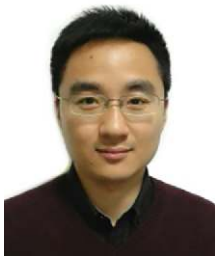
Author contributions Chen Y and Qin Z designed the project; Qin Z, Wang M, and Li R performed the experiments; Chen Y and Qin Z wrote the paper. All authors contributed to the general discussion.

Conflict of interest The authors declare no conflict of interest.

Supplementary information Supporting data are available in the online version of the paper.



Zhixiao Qin received his bachelor degree from Xi'an Jiaotong University in 2013. He is currently a PhD student at Xi'an Jiaotong University. His research interests focus on photocatalytic and photoelectrochemical water splitting.



Yubin Chen is an associate professor at Xi'an Jiaotong University. He received his bachelor degree in 2007 and PhD degree in 2013 from Xi'an Jiaotong University. From 2011 to 2012, he studied at Case Western Reserve University as a visiting scholar. His current research interests focus on photocatalysis, water splitting and functional nanomaterials for energy conversion.

新型磷化铜/氮化碳p-n异质结光催化剂的太阳能产氢性能研究

秦知校, 王朦胧, 李锐, 陈玉彬*

摘要 开发高效的异质结光催化剂促进电荷的分离和转移对提高太阳能光催化产氢性能至关重要. 本文采用p型的磷化铜和n型的氮化碳形成p-n结来促进电荷分离和转移, 从而提高光催化产氢性能. 与纯的氮化碳相比, 磷化铜/氮化碳p-n异质结光催化剂的产氢性能提高了95倍, 在420纳米处的量子效率达到2.6%. 我们通过荧光光谱, 表面光电压谱以及电化学测试进一步分析反应机理, 发现显著提高的光催化产氢性能应归因于p-n异质结光催化剂中高效的电荷分离. 本研究表明形成p-n异质结是开发高效光催化剂的一种有效途径.